catalysts

MDPI

Article

Carbon Monoxide and Propylene Catalytic Oxidation Activity of Noble Metals (M = Pt, Pd, Ag, and Au) Loaded on the Surface of $Ce_{0.875}Zr_{0.125}O_2$ (110)

Chenxi Zhang [1,2], Xuesong Cao [2], Lili Guo [1], Zhihao Fang [1], Di Feng [1,*] and Xiaomin Sun [2]

[1] Shandong Provincial University Laborator for Protected Horticulture, Weifang University of Science and Technology, Weifang 262700, China; sdzhangcx@gmail.com (C.Z.); 13279293652@163.com (L.G.); wfsgfzh@163.com (Z.F.)

[2] Environment Research Institute, Shandong University, Qingdao 266200, China; xuesongcao@mail.sdu.edu.cn (X.C.); sxmwch@sdu.edu.cn (X.S.)

* Correspondence: fengdi2008sunny@163.com

Abstract: With the advances in engine technology, the exhaust gas temperature of automobiles has further reduced, which in turn leads to an increase in the emissions of carbon monoxide (CO) and hydrocarbons (HCs). In order to understand the influence of CeO_2-based catalysts loaded with different noble metals on the catalytic oxidation activity of CO and HCs, this study constructed catalyst models of $Ce_{0.875}Zr_{0.125}O_2$ (100) surfaces loaded with Pt, Pd, Ag, and Au. The electronic density and state density structures of the catalysts were analyzed, and the reaction energy barriers for CO oxidation and C_3H_6 dehydrogenation oxidation on the catalyst surfaces were also calculated. Furthermore, the activity sequences of the catalysts were explored. The results revealed that after loading Pt, Pd, Ag, and Au atoms onto the catalyst surfaces, these noble metal atoms exhibited strong interactions with the catalyst surfaces, and electron transfer occurred between the noble metal atoms and the catalyst surfaces. Loading with noble metals can enhance the catalytic activity of CO oxidation, but it has little effect on the dehydrogenation oxidation of C_3H_6. Of the different noble metals, loading with Pd exhibits the best catalytic activity for both CO and C_3H_6 oxidation. This study elucidated the influence of noble metal doping on the catalytic activity of catalysts at the molecular level, providing theoretical guidance for the design of a new generation of green and efficient catalysts.

Keywords: noble metal; $Ce_{0.875}Zr_{0.125}O_2$ (100) surface; CO oxidation; C_3H_6 dehydrogenation oxidation; catalytic activity

check for updates

Citation: Zhang, C.; Cao, X.; Guo, L.; Fang, Z.; Feng, D.; Sun, X. Carbon Monoxide and Propylene Catalytic Oxidation Activity of Noble Metals (M = Pt, Pd, Ag, and Au) Loaded on the Surface of $Ce_{0.875}Zr_{0.125}O_2$ (110). *Catalysts* **2023**, *13*, 1505. https://doi.org/10.3390/catal13121505

Academic Editor: Laura Orian

Received: 4 November 2023
Revised: 29 November 2023
Accepted: 4 December 2023
Published: 11 December 2023

1. Introduction

In recent years, with the increasingly stringent automotive exhaust emission standards worldwide, higher requirements have been put forward for improving fuel efficiency and reducing exhaust emissions [1,2]. In order to improve fuel efficiency, low-temperature combustion (LTC) and cold start technologies have been adopted, which reduce the emissions of NO_x and particulate matter (PM) due to the decrease in exhaust temperature, but increase the emissions of CO and hydrocarbons (HCs) [3,4]. Therefore, finding appropriate catalysts and improving the efficiency of CO and HC elimination is an important task.

Cerium oxide (CeO_2) has been widely used in the oxidation reactions of CO and HC due to its unique redox properties [5,6]. The state of Ce can easily shuttle between Ce^{3+} and Ce^{4+}, which gives CeO_2 excellent oxygen-storage capacity (OSC) and a large number of surface oxygen vacancies [7,8]. To improve the thermal stability and low-temperature redox performance of CeO_2, it is often doped with zirconium dioxide (ZrO_2) to form a Ce-Zr mixed oxide, namely a $Ce_xZr_{1-x}O_2$ solid solution [9–11]. Compared with pure CeO_2 catalysts, the thermal stability and oxygen-storage performance of $Ce_xZr_{1-x}O_2$ solid solutions have been greatly improved.

Studies have shown that the addition of noble metals can improve the activities of CeO_2 and $Ce_xZr_{1-x}O_2$ solid solutions in oxidation reactions [12]. Ag can enhance the OSC of CeO_2, which supports the oxidation ability of CeO_2 [13]. Dou et al. prepared a series of Ag/CeO_2 catalysts using incipient wetness impregnation for C_3H_6 oxidation experiments [14]. Their results show that the participation of Ag-CeO_2 reduces the ignition temperature of C_3H_6 by more than 50 °C and increases the conversion rate by 36.1%. A single Au atom on the CeO_2 (110) surface promotes the oxidation of CO by the surface O atoms of CeO_2 [15]. Pt/CeO_2 can enhance the catalytic activity and stability of particulate matter oxidation [16]. Li et al. successfully synthesized a $Pt@CeO_{2x}/ZrO_2$ catalyst, which exhibited excellent catalytic activity for soot combustion [17]. Pd-CeO_2 catalyst is a good cold start catalyst, showing lower ignition temperatures during CO and light HC ignition [18,19]. Shen et al. prepared Pd/CeO_2 catalysts with different Pd loading ratios and found that the oxidation performance of CO and C_3H_6 improved with increasing Pd loading [2]. Yoo et al. examined the effects of the Pd precursor on the activities and properties of Pd/CeO_2 catalysts, concluding that highly dispersed Pd can promote the CO oxidation reaction [20]. However, the relationship between catalytic oxidation activity and different noble metals is still unclear, and there are no reports in the literature on the activity sequences of various noble metals loaded onto CeO_2.

In recent years, using theoretical calculation methods to study the properties of catalysts and to explain experimental phenomena has become a popular technical means [21–25]. Although experiments have used advanced instruments, such as scanning transmission electron microscopy (STEM), X-ray absorption near edge structure (XANES), extended X-ray absorption fine structure (EXAFS), and Fourier transform infrared (FTIR) spectroscopy, they still have not been able to clearly explain the electronic structure of catalysts [26]. By applying density functional theory (DFT) calculations, the precise structure of noble metal single atoms anchored on the surfaces of CeO_2-based catalysts can be obtained. By calculating the potential barriers of catalytic oxidation reactions, the activity sequences of catalysts can be obtained more intuitively.

The aim of the present study is to understand the CO and HC catalytic oxidation activity of different noble metals (M = Pt, Pd, Ag, and Au) on CeO_2-based catalysts for oxidation reactions. For this purpose, surface models of Pt, Pd, Ag, and Au supported by $Ce_{0.875}Zr_{0.125}O_2$, which showed the most promising surface lattice oxygen release activity of all $Ce_xZr_{1-x}O_2$ solid solutions, were constructed [27]. Then, the electron density and density of states (DOS) structures of the catalysts were analyzed to understand the electronic structure characteristics of the noble-metal-doped catalysts. The reaction energy barriers for the catalytic oxidation of CO and C_3H_6, a typical HC in gasoline vehicle exhaust, were calculated to explore the activity sequences of the catalysts. This elucidated the influence of the structural characteristics of the catalysts on their catalytic activity at the molecular level, which has theoretical guiding significance for the design of a new generation of green and efficient catalysts.

2. Results and Discussion

For CeO_2-supported catalysts, the (110) surface is catalytically more active than the (111) and (100) surfaces and it is often chosen to study the reaction mechanism [27,28]. Thus, the $Ce_{0.875}Zr_{0.125}O_2$ (110) surface was selected to further investigate the catalytic activity of catalysts loaded with noble metals (M = Pt, Pd, Ag, and Au).

The surfaces of $Ce_{0.875}Zr_{0.125}O_2$ (110) loaded with Pt, Pd, Ag, and Au atom catalysts are shown in Figure 1. The Pt, Pd, Ag, and Au single atoms are adsorbed onto the double O-bridge sites of the $Ce_{0.875}Zr_{0.125}O_2$ (110) surface, which has been proven to have the lowest adsorption energy [28,29]. The surface models of $Pt_1/Ce_{0.875}Zr_{0.125}O_2$ (110), $Pd_1/Ce_{0.875}Zr_{0.125}O_2$ (110), $Ag_1/Ce_{0.875}Zr_{0.125}O_2$ (110), and $Au_1/Ce_{0.875}Zr_{0.125}O_2$ (110) all consist of four atomic layers, with the bottom two layers of atoms fixed and the top two layers of atoms and the adsorbed Pt, Pd, Ag, and Au single atoms unfixed. The

thickness of the vacuum layer in the models is 15 Å, to eliminate the interactions between the lattice and the lattice in the *z* direction.

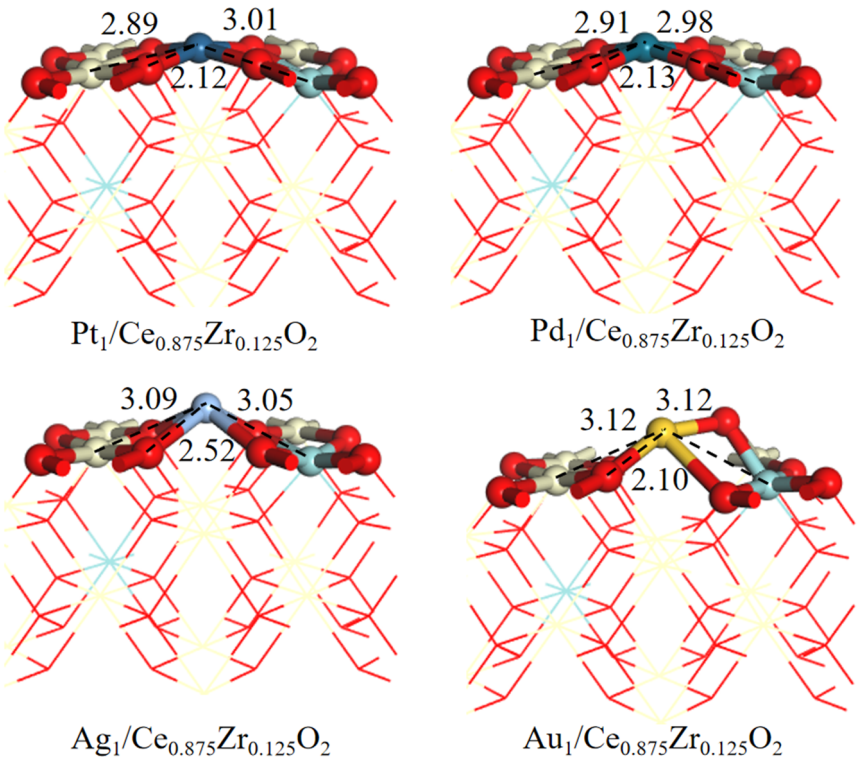

Figure 1. Optimized structure models of $Pt_1/Ce_{0.875}Zr_{0.125}O_2$, $Pd_1/Ce_{0.875}Zr_{0.125}O_2$, $Ag_1/Ce_{0.875}Zr_{0.125}O_2$, and $Au_1/Ce_{0.875}Zr_{0.125}O_2$ (110) surfaces.

2.1. Structural Characteristics of the Catalysts

The structures and binding energies of the (Pt, Pd, Ag, and Au)$_1$/$Ce_{0.875}Zr_{0.125}O_2$ catalysts were analyzed. As shown in Figure 1, on the $Pt_1/Ce_{0.875}Zr_{0.125}O_2$ surface, the distances between the Pt atom and the surface O, Ce, and Zr atoms are 2.12, 2.89, and 3.01 Å, respectively. The Pt atom is anchored at the quadruple O vacancies on the $Ce_{0.875}Zr_{0.125}O_2$ (110) surface. Figure 2a,b show the electron density of the $Pt_1/Ce_{0.875}Zr_{0.125}O_2$ surface. The electron orbitals of Pt overlap with those of the $Ce_{0.875}Zr_{0.125}O_2$ (110) surface, indicating that the Pt atoms are tightly bound to the $Ce_{0.875}Zr_{0.125}O_2$ (110) surface through chemical adsorption. The large binding energies of the Pt atoms on the $Ce_{0.875}Zr_{0.125}O_2$ (110) surface (−4.16 eV) also indicate that Pt can be stably adsorbed on the (110) surface of $Ce_{0.875}Zr_{0.125}O_2$. In addition, as shown in Table 1, the Mulliken charge of the Pt atom on the surface of $Pt_1/Ce_{0.875}Zr_{0.125}O_2$ is 0.14 e, indicating a transfer of 0.14 e from the Pt atom to the surface. The same method was used to analyze the surface of $Pd_1/Ce_{0.875}Zr_{0.125}O_2$ (Figures 1 and 2c,d). The bond length between Pd and the surface O is 2.13 Å, while the Pd–Ce and Pd–Zr distances are 2.91 and 2.98 Å, respectively, which are similar to the structure of $Pt_1/Ce_{0.875}Zr_{0.125}O_2$. The binding energy between Pd and the surface is −3.07 eV, and the electron densities of the Pd and surface atoms also overlap with each other, with 0.21 e of the Mulliken charge of Pd transferred to the surface. The binding energy between Ag atoms and the $Ce_{0.875}Zr_{0.125}O_2$ (110) surface is −1.77 eV, which is lower than the adsorption energies of Pt and Pd atoms. Additionally, the distances between the Ag and surface O, Ce, and Zr atoms are relatively large: 2.52, 3.09, and 3.05 Å, respectively. The electron density map of the $Ag_1/Ce_{0.875}Zr_{0.125}O_2$ (110) surface indicates that orbital overlap is still present between the Ag atoms and the surface, with the Ag atoms transferring a large number of electrons (0.25 e) to the surface. The geometric model of the $Au_1/Ce_{0.875}Zr_{0.125}O_2$ (110) surface is shown in Figure 1. The adsorption of Au leads to the lifting of the O atoms connected to the Ce and Zr atoms. The distances between the Au and surface O, Ce, and Zr

atoms are 2.10, 3.12, and 3.12 Å, respectively, and the binding energy between Au and the surface is also low (−1.99 eV). Orbital overlap is also found between the electron density of Au atoms and the electron density of the surface, as the binding energy is approximately −2.00 eV, indicating strong chemical adsorption, although this value is lower than those of Pt and Pd.

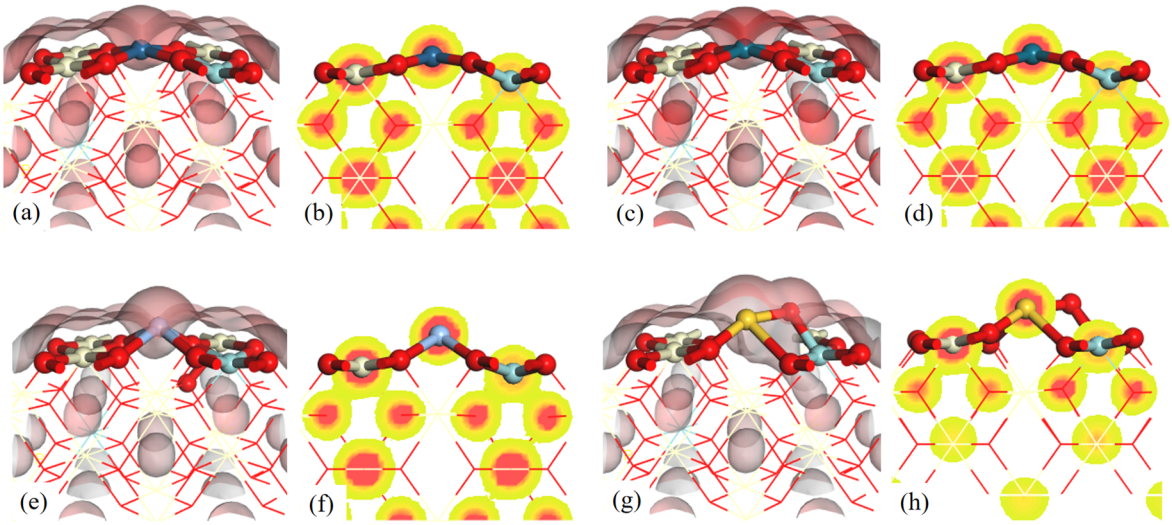

Figure 2. (**a**) Three-dimensional view of deformation electron density and (**b**) two-dimensional view of deformation electron density of the $Pt_1/Ce_{0.875}Zr_{0.125}O_2$ (110) surface. (**c**) Three-dimensional view of deformation electron density and (**d**) two-dimensional view of deformation electron density of the $Pd_1/Ce_{0.875}Zr_{0.125}O_2$ (110) surface. (**e**) Three-dimensional view of deformation electron density and (**f**) two-dimensional view of deformation electron density of the $Ag_1/Ce_{0.875}Zr_{0.125}O_2$ (110) surface. (**g**) Three-dimensional view of deformation electron density and (**h**) two-dimensional view of deformation electron density of the $Au_1/Ce_{0.875}Zr_{0.125}O_2$ (110) surface.

Table 1. Binding energy and Mulliken charge of M (Pt, Pd, Ag, and Au) on the $Ce_{0.875}Zr_{0.125}O_2$ (110) surface.

Noble Metal	E_{ads} (eV)	Mulliken (e)
Pt	−4.16	0.14
Pd	−3.07	0.21
Ag	−1.77	0.25
Au	−1.99	0.02

In general, the results indicate that the Pt, Pd, Ag, and Au atoms all have strong interactions with the surface, and electron transfer takes place between them and the surface. The binding energies of Pt and Pd atoms are higher than those of Ag and Au atoms. Further calculations were conducted of the density of states of the M (Pt, Pd, Ag, and Au)$_1/Ce_{0.875}Zr_{0.125}O_2$ (110) surfaces, and the results are shown in Figure 3. As shown in Figure 3, no apparent change occurs after the adsorption of all the orbitals, indicating that the $Ce_{0.875}Zr_{0.125}O_2$ (110) surface can remain stable after noble metal adsorption. In addition, compared with the $Ce_{0.875}Zr_{0.125}O_2$ (110) surface, all the orbitals of the $M/Ce_{0.875}Zr_{0.125}O_2$ (110) surfaces shift toward lower energy levels after noble metal loading, indicating the formation of a more stable configuration. Among them, orbital movement after Pd adsorption is the most significant.

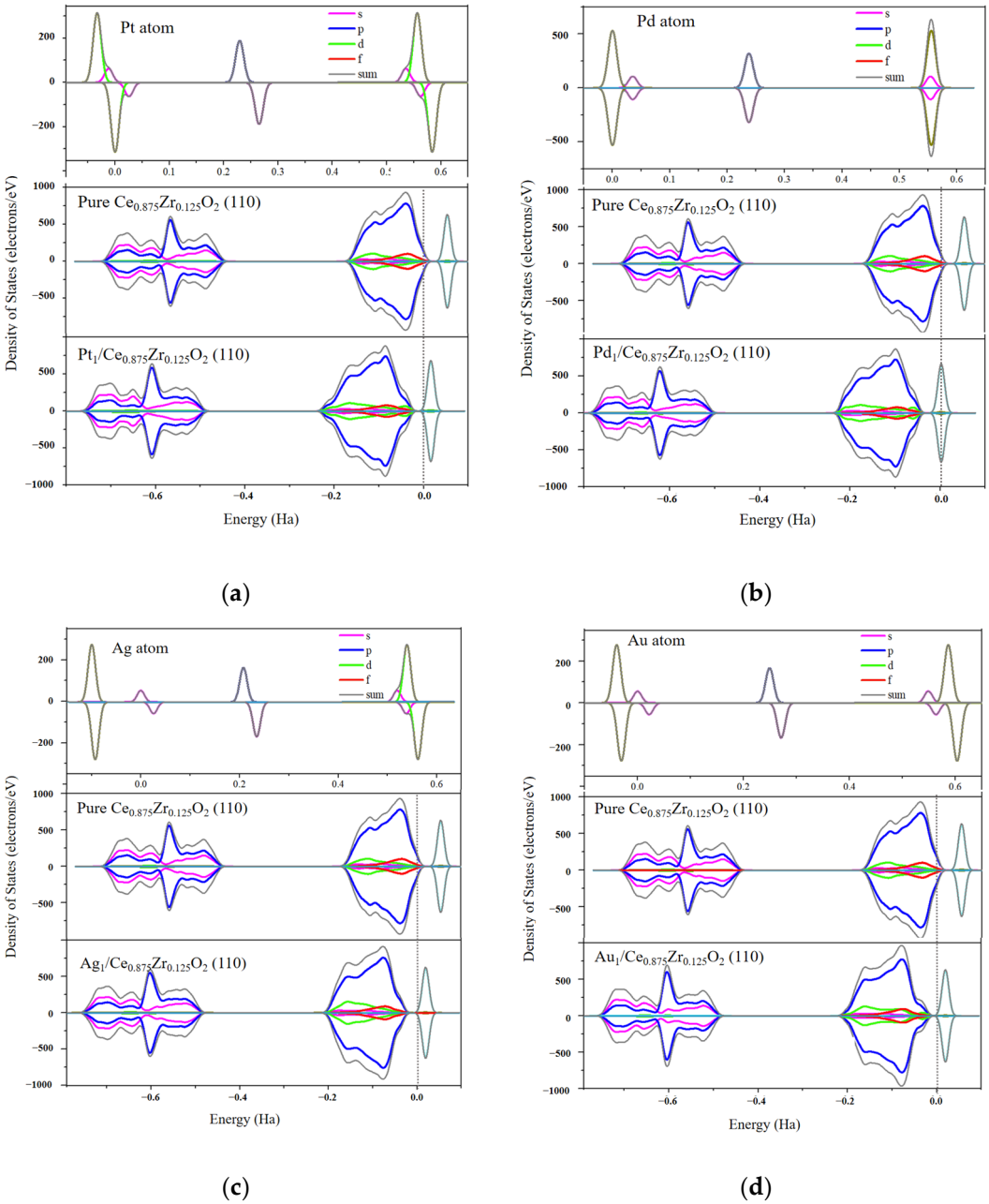

Figure 3. Total density of states and partial density of states of (**a**) $Pt_1/Ce_{0.875}Zr_{0.125}O_2$, (**b**) $Pd_1/Ce_{0.875}Zr_{0.125}O_2$, (**c**) $Ag_1/Ce_{0.875}Zr_{0.125}O_2$, and (**d**) $Au_1/Ce_{0.875}Zr_{0.125}O_2$ (110) surfaces compared with that of the clean (110) surfaces and the electron states of the free metal atoms.

The $Pd_1/Ce_{0.875}Zr_{0.125}O_2$, $Ag_1/Ce_{0.875}Zr_{0.125}O_2$, and $Au_1/Ce_{0.875}Zr_{0.125}O_2$ surfaces exhibit the same trend.

2.2. Oxidation of C_3H_6 Catalyzed by M/$Ce_{0.875}Zr_{0.125}O_2$ Catalysts

As a common hydrocarbon (HC) in automotive exhaust emissions, propylene (C_3H_6) is often used as a typical gas molecule to investigate the activity of three-way catalysts and is also a gas that needs to be eliminated from automotive exhaust emissions. The exploration of the oxidation reaction of C_3H_6 on the M (Pt, Pd, Ag, and Au)$_1$/$Ce_{0.875}Zr_{0.125}O_2$ (100) surfaces can elucidate the C_3H_6 oxidation activity of CeO_2-supported catalysts and identify the most suitable catalyst for eliminating HCs.

The complete catalytic oxidation of C_3H_6 proceeds via a complex reaction process. The first C–H bond activation step always initiates the entire process and is generally thought

of as a crucial step in C_3H_6 oxidation [30]. Two different C–H bonds, namely the C_{sp3}–H bond and C_{sp2}–H bond, are considered as active sites for oxidation reactions. Among them, the activation of the C_{sp3}–H bond has been proven to be a favorable pathway [30]. This is also consistent with the study of Yang et al., who found that propene is adsorbed onto Pt (111) with the C atoms sp^3-hybridized [31]. Therefore, this study utilized the C_{sp3}–H bond cleavage of C_3H_6 molecules on the $M/Ce_{0.875}Zr_{0.125}O_2$ surface catalyst as a probe reaction to investigate the effect of noble metal doping on the oxidation activity of C_3H_6 at the molecular level. Figure 4 illustrates the reaction mechanism of the oxidation of C_3H_6 by $Pt_1/Ce_{0.875}Zr_{0.125}O_2$. Firstly, C_3H_6 tends to adsorb onto surface lattice O atoms with higher E_{ads} values [30]. There are two types of surface lattice O atoms on the (110) surface of $Pt_1/Ce_{0.875}Zr_{0.125}O_2$: lattice O ($O_A$) connected to two Ce atoms, and lattice O (O_B) connected to one Ce and one Zr atom. The activities of O_A and O_B in the oxidation of C_3H_6 are different. The adsorption energy of the H atoms of the C_3H_6 methyl group at O_A sites is −0.77 eV, and the H–O_A bond length is 2.82 Å. Subsequently, the C_{sp3}–H bonds of C_3H_6 break, and the H atoms move toward O_A. In TS-1, the H–O_A bond length is 1.30 Å, and the C_{sp3}–H bond length increases from the original 1.11 Å to 1.54 Å. Finally, $CH_2{=}CHCH_2$* and a surface hydroxyl group (–O_AH) are formed. The energy barrier and enthalpy of the reaction are 1.19 and 0.94 eV, respectively. It is worth noting that the ΔE of C_3H_6 dehydrogenation oxidation is positive and the process requires additional energy, which is not favorable in terms of thermodynamics. The oxidation reaction of C_3H_6 follows the same steps at the O_B sites, where the adsorption energy of C_3H_6 is −0.78 eV, slightly lower than that at the O_A sites. In addition, Valcárcel et al. studied the adsorption of propene on Pt (111) surfaces using both slab and cluster models and density functional theory methods; the predicted binding energy of C_3H_6 on Pt (111) ranges from −0.9 to −0.10 eV [32]. This indicates that it becomes easier to adsorb C_3H_6 after Pt loading of the $Ce_{0.875}Zr_{0.125}O_2$ (110) surface. The E_a and ΔE of the reaction are 0.81 and 0.68 eV, respectively. The energy barrier is lower than that at the O_A sites, indicating that the oxidation of C_3H_6 is more likely to occur at the O_B sites of the $Pt_1/Ce_{0.875}Zr_{0.125}O_2$ (110) surface.

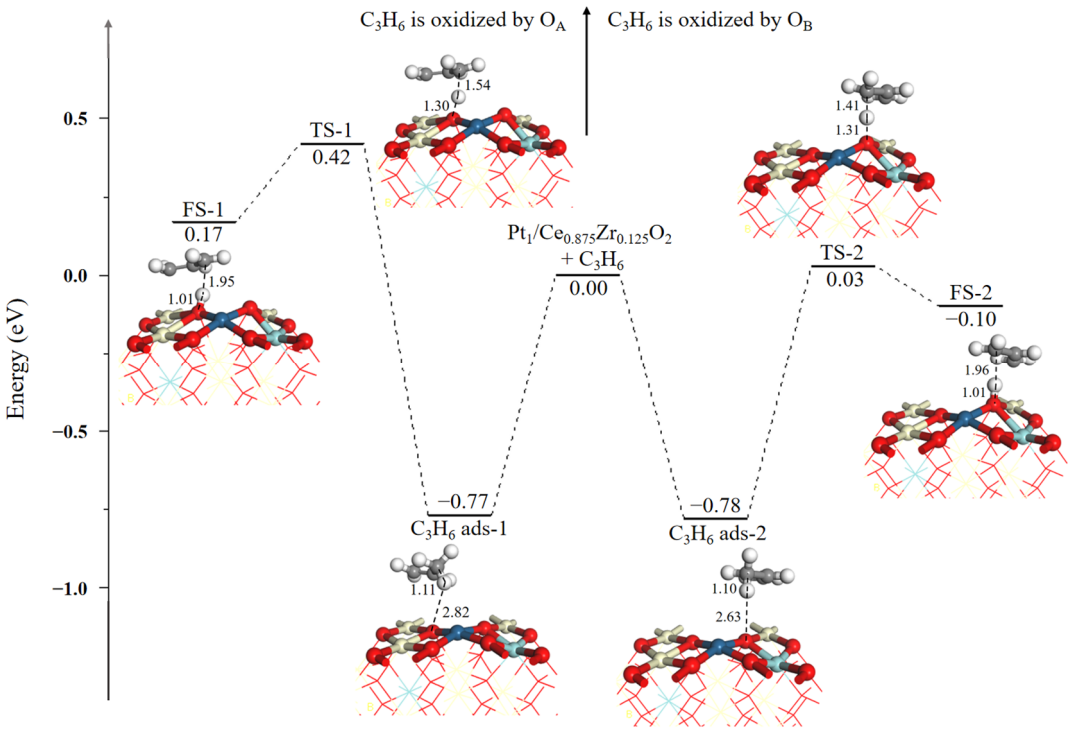

Figure 4. Calculated energy profile and corresponding optimized configurations of reactants, transition states (TS), and products (FS) of the activation of the C_{sp3}–H bond of C_3H_6 on the $Pt_1/Ce_{0.875}Zr_{0.125}O_2$ (110) surface.

The reaction path of C_3H_6 oxidation on the $Pd_1/Ce_{0.875}Zr_{0.125}O_2$ (110) surface is similar to that on the $Pt_1/Ce_{0.875}Zr_{0.125}O_2$ (110) surface. As shown in Figure S1, the adsorption energies of C_3H_6 at the O_A (C_3H_6 ads-3) and O_B (C_3H_6 ads-4) sites on the $Pd_1/Ce_{0.875}Zr_{0.125}O_2$ (110) surface are −0.76 and −0.58 eV, respectively. The H–O_A and H–O_B bond lengths are 2.68 and 2.93 Å, respectively. The energy barriers that need to be overcome in the dehydrogenation oxidation reaction are 1.03 eV (TS-3) and 0.49 eV (TS-4), and the reaction energies are 0.87 and 0.44 eV, respectively. The reaction energy barrier for extracting H from the O_B sites is significantly lower than that from the O_A sites.

The mechanisms of the oxidation reaction of C_3H_6 molecules on the $Ag_1/Ce_{0.875}Zr_{0.125}O_2$ (110) and $Au_1/Ce_{0.875}Zr_{0.125}O_2$ (110) surfaces were also calculated and are shown in Figures S2 and S3, respectively. The reaction energy barriers for the O_A and O_B oxidation of C_3H_6 on the (110) surface of $Ag_1/Ce_{0.875}Zr_{0.125}O_2$ are 1.19 eV (TS-5) and 0.87 eV (TS-6), respectively. The reaction energy barriers for the O_A and O_B oxidation of C_3H_6 on the (110) surface of $Au_1/Ce_{0.875}Zr_{0.125}O_2$ are 1.50 eV (TS-7) and 0.89 eV (TS-8), respectively. A comparison of these values shows that, on the same catalyst surface, the reaction energy barrier at O_B sites is lower than that at O_A sites, indicating that the catalytic activity of O_B sites in the oxidative dehydrogenation of C_3H_6 is higher than that of O_A sites. The energy barrier for the oxidation of C_3H_6 at the O_B sites of the $Pd_1/Ce_{0.875}Zr_{0.125}O_2$ (110) surface is the lowest (0.49 eV), indicating the highest catalytic activity for the oxidation of C_3H_6, which makes it the optimal catalyst surface. The activity of (Pt, Pd, Ag, and Au)$_1/Ce_{0.875}Zr_{0.125}O_2$ in the oxidation of C_3H_6 decreases in the order Pd > Ag > Au > Pt.

However, compared with the calculated energy barrier (0.45 eV) for C_3H_6 oxidation on the $Ce_{0.875}Zr_{0.125}O_2$ (110) surface discussed in the previous section, the addition of noble metals does not reduce the energy barrier for the C_3H_6 dehydrogenation oxidation reaction [30]. This indicates that the addition of Pt, Pd, Ag, and Au single atoms does not enhance the activity of $Ce_{0.875}Zr_{0.125}O_2$ in the oxidation of C_3H_6.

2.3. CO Oxidation Catalyzed by M/$Ce_{0.875}Zr_{0.125}O_2$ Catalysts

There is a general consensus on the detailed mechanism of CO oxidation on the surface of CeO_2, termed the Mars–van Krevelen (MvK) mechanism [5,33]. CO extracts a surface lattice O from the CeO_2 surface to form CO_2, which results in the creation of oxygen vacancies (O_V), which is then supplemented with gas-phase O_2 to complete the catalytic cycle.

This study employed the reaction of CO-capturing surface lattice O_A, which has been proven to be the optimal site, as a probe reaction to investigate the catalytic activity of different noble metals on $Ce_{0.875}Zr_{0.125}O_2$ catalysts for CO oxidation [27]. Figures 5 and S4 show the energy barrier diagrams and structural models of the corresponding reactants, transition states, and products for the oxidation of CO on the surfaces of $Pt_1/Ce_{0.875}Zr_{0.125}O_2$, $Pd_1/Ce_{0.875}Zr_{0.125}O_2$, $Ag_1/Ce_{0.875}Zr_{0.125}O_2$, and $Au_1/Ce_{0.875}Zr_{0.125}O_2$. CO is adsorbed at the O_A sites of the $Pt_1/Ce_{0.875}Zr_{0.125}O_2$ (110) surface, with a CO–O_A distance of 2.83 Å and an adsorption energy of −0.44 eV. Subsequently, CO migrates toward O_A, resulting in the CO−O_A distance of TS-9 being shortened to 1.49 Å, with a C–O–O_A angle of 120°. Finally, CO extracts the surface lattice oxygen according to the MvK mechanism, generating CO_2 and surface O_V. The activation energy barrier of the pathway is 0.71 eV and the reaction enthalpy is −0.37 eV.

The adsorption energy of CO at the O_A sites of the $Pd_1/Ce_{0.875}Zr_{0.125}O_2$ (110) surface is −0.44 eV, and the distance between the O atom of the CO group and the surface O_A lattice atoms is 2.93 Å. Subsequently, CO extracts the O_A atom, and the O–O_A distance is shortened to 1.24 Å (TS-10); the Pd–O_A distance increases from 2.12 to 2.60 Å (TS-10), ultimately generating a $Pd_1/Ce_{0.875}Zr_{0.125}O_2$ defective surface containing an oxygen vacancy and CO_2. The activation energy barrier that needs to be overcome in this process is 0.49 eV and the reaction enthalpy is −0.50 eV. The adsorption energy of CO on the $Ag_1/Ce_{0.875}Zr_{0.125}O_2$ surface is −0.40 eV; the reaction has an energy barrier of 1.05 eV (TS-11) and releases 0.63 eV

of heat. The adsorption energy of CO on the surface of $Au_1/Ce_{0.875}Zr_{0.125}O_2$ is −0.43 eV; the reaction energy barrier and enthalpy are 0.64 eV (TS-12) and −0.50 eV, respectively.

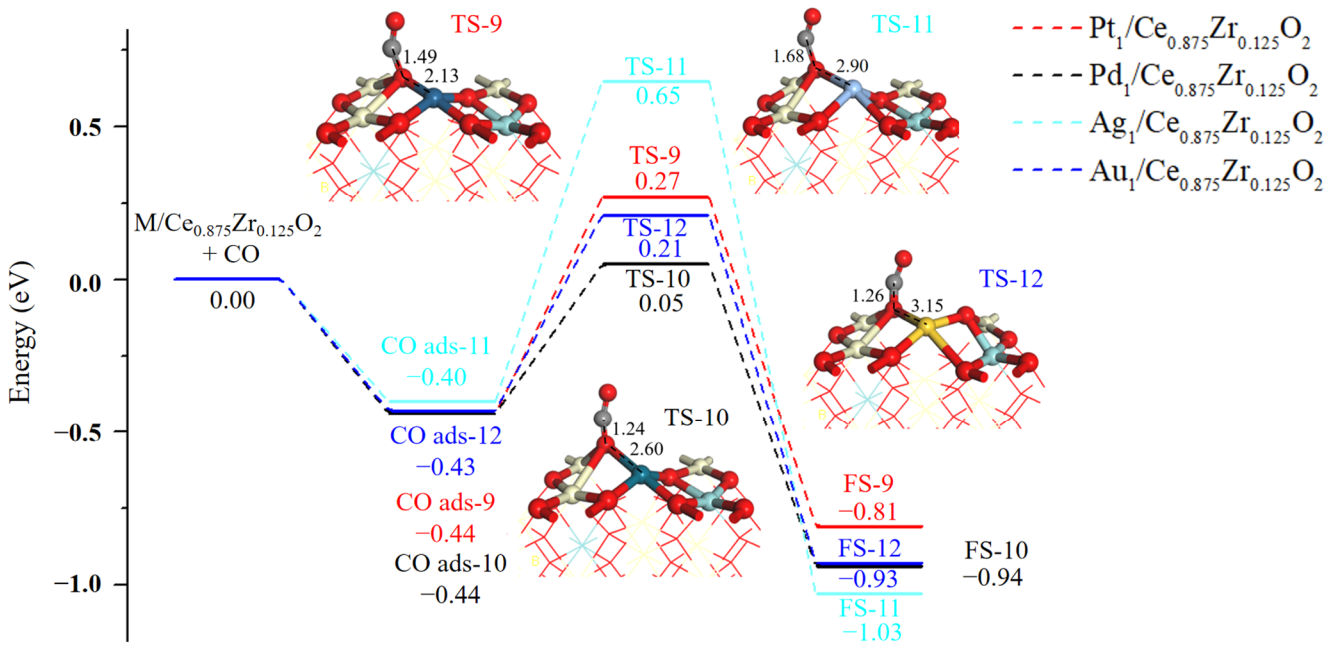

Figure 5. Calculated energy profiles of the CO oxidation reaction on the $Pt_1/Ce_{0.875}Zr_{0.125}O_2$, $Pd_1/Ce_{0.875}Zr_{0.125}O_2$, $Ag_1/Ce_{0.875}Zr_{0.125}O_2$, and $Au_1/Ce_{0.875}Zr_{0.125}O_2$ (110) surfaces.

The comparison of the reaction energy barriers for CO oxidation on the $M/Ce_{0.875}Zr_{0.125}O_2$ (100) surfaces shows that the surface of $Pd_1/Ce_{0.875}Zr_{0.125}O_2$ (100) has the lowest energy barrier for activating CO (0.49 eV), which is considerably lower than the experimental (1.8–2.1 eV) and theoretical values (1.7–1.8 eV) for CO oxidation on CeO_2 surface [34,35]. It is also lower than the reaction energy barrier (0.90 eV) for CO oxidation on the $Ce_{0.875}Zr_{0.125}O_2$ (110) surface and CO oxidation on the Pd_1/CeO_2 (110) surface (0.95 eV) [27,36]. Therefore, the addition of Pt, Pd, Ag, and Au single atoms leads to an increase in catalytic activity for CO oxidation, with the $Pd_1/Ce_{0.875}Zr_{0.125}O_2$ surface having the highest level of activity.

3. Computational Methods and Parameter Settings

The DMol^3 module of the Materials Studio software package was used to optimize the structure of all single-atom models [37,38]. The GGA–PBE exchange-correlation functional and the DND basis set were adopted in the calculations [39]. Ce ($4f^1$, $5s^2$, $5p^6$, $5d^1$, and $6s^2$) and Zr ($4s^2$, $4p^6$, $4d^2$, and $5s^2$) electrons were treated as valence electrons using the effective core potential (ECP) method, while O, C, and N atoms were treated using the all-electron method to increase the calculation speed [40]. SCF and Fermi smoothing were set to 1×10^{-5} and 0.005 Ha, respectively, to accelerate the convergence. The orbital cutoff radius and k-point precision were set to 5.0 Å and (1 × 2 × 1), respectively. The convergence thresholds for the energy, maximum force, and maximum displacement were 2×10^{-5} Ha, 0.004 Ha/Å, and 0.005 Å, respectively.

To properly account for the band structure of CeO_2, Hubbard U corrections were applied to f electrons in some calculations [41,42]; however, previous research studies have indicated that plain DFT calculations could provide reasonable predictions of reduction energies, even better than those using DFT + U [35,43]. To ascertain the importance of the U parameter, we calculated the oxygen vacancy formation energies on the $Ce_{0.875}Zr_{0.125}O_2$ (110) surface when U = 5 eV and without incorporating U. The results show that the vacancy formation energy without incorporating U (10.88 kcal mol^{-1}) is within 1% of that when U = 5 eV (10.98 kcal mol^{-1}). Hence, the DFT + U method is not considered in this work.

The calculation formula for the adsorption energy (E_{ads}) of the catalyst surfaces is as follows:

$$E_{ads} = E_{substrate+adsorbate} - E_{substrate} - E_{adsorbate} \quad (1)$$

where $E_{substrate+adsorbate}$ is the total energy of the molecule or atom adsorbed on the catalyst surface; $E_{substrate}$ is the energy of the catalyst surface; and $E_{adsorbate}$ is the optimized energy of the molecule or atom. A more negative value of E_{ads} indicates a stronger binding between the noble metal atom and the catalyst surface. The transition state (TS) of the reaction is found using the LST/QST method, and the rationality of the TS is verified by calculating the imaginary frequency of the structure [44].

The calculation formulas for reaction heat (ΔE) and reaction barrier (E_a) are as follows:

$$\Delta E = E_{FS} - E_{IS} \quad (2)$$

$$E_a = E_{TS} - E_{IS} \quad (3)$$

where E_{IS} is the total energy of the reactant (IS); E_{TS} is the energy of the transition state (TS); and E_{FS} is the total energy of the product (FS).

4. Conclusions

Based on DFT calculations, this work developed a structural model of the (110) surfaces of $M/Ce_{0.875}Zr_{0.125}O_2$ catalysts and systematically determined the structural characteristics of the (Pt, Pd, Ag, and Au)$_1$/$Ce_{0.875}Zr_{0.125}O_2$ (110) surfaces as well as their catalytic activities for C_3H_6 oxidation and CO oxidation. This study provides a better understanding of the CO and C_3H_6 catalytic activity of different noble metals loaded onto CeO_2-based catalysts for the purification of automotive exhaust emissions. Based on the results of the DFT calculations, the following conclusions can be drawn:

1. Pt, Pd, Ag, and Au atoms can stably bind to the (110) surface of $Ce_{0.875}Zr_{0.125}O_2$. Electron density overlaps and electron-transfer effects are observed between single atoms and the surface, indicating a strong degree of interaction;
2. The activity of (Pt, Pd, Ag, and Au)$_1$/$Ce_{0.875}Zr_{0.125}O_2$ in the oxidation of C_3H_6 decreases in the order Pd > Ag > Au > Pt. Moreover, the activity of surface O_B sites in the oxidative dehydrogenation of C_3H_6 is higher than that of O_A sites. Compared with the energy barrier for the oxidation of C_3H_6 on the (110) surface of $Ce_{0.875}Zr_{0.125}O_2$ (0.45 eV), the addition of noble metals does not reduce the reaction energy barrier for C_3H_6 dehydrogenation oxidation;
3. The catalytic activity of (Pt, Pd, Ag, and Au)$_1$/$Ce_{0.875}Zr_{0.125}O_2$ in the oxidation of CO decreases in the order Pd > Au > Pt > Ag. The (110) surface of Pd_1/$Ce_{0.875}Zr_{0.125}O_2$ has the lowest energy barrier (0.49 eV) in the activation of CO, and the loading of single-atom Pt, Pd, Ag, and Au can increase the activity of $Ce_{0.875}Zr_{0.125}O_2$ during CO oxidation.

Supplementary Materials: The following are available online at: https://www.mdpi.com/article/10.3390/catal13121505/s1, Figure S1: Calculated energy profile and corresponding optimized configurations of reactants, transition states, and products of the activation of the C_{sp3}–H bond of C_3H_6 on the Pt_1/$Ce_{0.875}Zr_{0.125}O_2$ (110) surface; Figure S2: calculated energy profile and corresponding optimized configurations of reactants, transition states, and products of the activation of the C_{sp3}–H bond of C_3H_6 on theAg_1/$Ce_{0.875}Zr_{0.125}O_2$ (110) surface; Figure S3: calculated energy profile and corresponding optimized configurations of reactants, transition states, and products of the activation of the C_{sp3}–H bond of C_3H_6 on the Au_1/$Ce_{0.875}Zr_{0.125}O_2$ (110) surface; Figure S4: the reactants, transition states, and products of the CO oxidation reaction on the Pt_1/$Ce_{0.875}Zr_{0.125}O_2$, Pd_1/$Ce_{0.875}Zr_{0.125}O_2$, Ag_1/$Ce_{0.875}Zr_{0.125}O_2$, and Au_1/$Ce_{0.875}Zr_{0.125}O_2$ (110) surfaces.

Author Contributions: Conceptualization, C.Z. and D.F.; data curation, X.C.; formal analysis, L.G.; funding acquisition, C.Z.; investigation, C.Z.; software, X.C. and Z.F.; supervision, D.F.; validation, C.Z. and X.S.; visualization, C.Z. and X.C.; writing—original draft, C.Z. and X.C.; writing—review and editing, D.F. All authors have read and agreed to the published version of the manuscript.

Funding: This research was funded by the National Natural Science Foundation of China, grant number 21607011, and the Key Research and Development Project of Shandong Province, grant number 2019GSF109021. The APC was funded by the Fundamental Research Funds of Weifang University of Science and Technology, grant number KJRC2022013.

Data Availability Statement: Data are contained within the article and supplementary materials.

Conflicts of Interest: The authors declare no conflict of interest.

References

1. Park, H.; Lee, E.J.; Woo, H.; Yoon, D.; Kim, C.H.; Jung, C.H.; Lee, K.B.; Lee, K.Y. Enhanced hydrothermal durability of Co_3O_4@CuO–CeO_2 Core-Shell catalyst for carbon monoxide and propylene oxidation. *Appl. Surf. Sci.* **2022**, *606*, 154916. [CrossRef]
2. Shen, M.; Wei, G.; Yang, H.; Wang, J.; Wang, X. Different selections of active sites for CO, C_3H_6, and $C_{10}H_{22}$ oxidation on Pd/CeO_2 catalysts. *Fuel* **2013**, *103*, 869–875. [CrossRef]
3. Lee, E.J.; Seo, Y.; Park, H.; Kim, M.J.; Yoon, D.; Choung, J.W.; Kim, C.H.; Choi, J.; Lee, K.Y. Development of etched SiO_2@Pt@ZrO_2 core-shell catalyst for CO and C_3H_6 oxidation at low temperature. *Appl. Surf. Sci.* **2022**, *575*, 151582. [CrossRef]
4. Wang, M.; Ma, P.; Wu, Z.; Chu, S.; Zheng, Y.; Zhou, Z.; Weng, W. Evolution of Pd chemical states and effects of C_3H_6 and H_2O on the CO oxidation over Pd/CeO_2 catalyst. *Appl. Surf. Sci.* **2022**, *599*, 153897. [CrossRef]
5. Wu, Z.; Li, M.; Overbury, S.H. On the structure dependence of CO oxidation over CeO_2 nanocrystals with well-defined surface planes. *J. Catal.* **2012**, *285*, 61–73. [CrossRef]
6. Rafaj, Z.; Krutel, J.; Nehasil, V. Oxygen exchange between catalyst and active support during CO oxidation on Rh/CeO_2(111) and Rh/CeO_2(110): Isotope labeled ^{18}O study. *J. Phys. Chem. C* **2021**, *125*, 15959–15966. [CrossRef]
7. Shuang, L.; Wu, X.D.; Duan, W.; Rui, R. Ceria-based catalysts for soot oxidation: A review. *J. Rare Earths* **2015**, *33*, 567–590.
8. Kim, M.J.; Han, G.-H.; Lee, S.H.; Jung, H.W.; Choung, J.W.; Kim, C.H.; Lee, K.-Y. CeO_2 promoted Ag/TiO_2 catalyst for soot oxidation with improved active oxygen generation and delivery abilities. *J. Hazard. Mater.* **2020**, *384*, 121341. [CrossRef]
9. Li, G.; Wang, Q.; Zhao, B.; Zhou, R. A new insight into the role of transition metals doping with CeO_2-ZrO_2 and its application in Pd-only three-way catalysts for automotive emission control. *Fuel* **2012**, *92*, 360–368. [CrossRef]
10. Aneggi, E.; de Leitenburg, C.; Dolcetti, G.; Trovarelli, A. Promotional effect of rare earths and transition metals in the combustion of diesel soot over CeO_2 and CeO_2-ZrO_2. *Catal. Today* **2006**, *114*, 40–47. [CrossRef]
11. Jonas, F.; Lebeau, B.; Siffert, S.; Michelin, L.; Poupin, C.; Cousin, R.; Josien, L.; Vidal, L.; Mallet, M.; Gaudin, P.; et al. Nanoporous CeO_2–ZrO_2 oxides for oxidation of volatile organic compounds. *ACS Appl. Nano Mater.* **2021**, *4*, 1786–1797. [CrossRef]
12. Lee, J.H.; Jo, D.Y.; Choung, J.W.; Kim, C.H.; Ham, H.C.; Lee, K.Y. Roles of noble metals (M = Ag, Au, Pd, Pt and Rh) on CeO_2 in enhancing activity toward soot oxidation: Active oxygen species and DFT calculations. *J. Hazard. Mater.* **2021**, *403*, 124085. [CrossRef] [PubMed]
13. Lee, J.H.; Lee, S.H.; Choung, J.W.; Kim, C.H.; Lee, K.-Y. Ag-incorporated macroporous CeO_2 catalysts for soot oxidation: Effects of Ag amount on the generation of active oxygen species. *Appl. Catal. B Environ.* **2019**, *246*, 356–366. [CrossRef]
14. Dou, C.; Lei, L.; Li, Z.; Meng, Z.; Wang, P. Ag-loaded CeO_2 catalysts for soot and C_3H_6 oxidation: Effect of Ag/Ce^{3+} on oxygen vacancies. *Therm. Sci. Engin. Prog.* **2023**, *38*, 101673. [CrossRef]
15. Song, W.; Hensen, E.J.M. Structure sensitivity in CO oxidation by a single Au atom supported on ceria. *J. Phys. Chem. C* **2013**, *117*, 7721–7726. [CrossRef]
16. Wei, Y.; Jiao, J.; Zhang, X.; Jin, B.; Zhao, Z.; Xiong, J.; Li, Y.; Liu, J.; Li, J. Catalysts of self-assembled Pt@$CeO_{2-\delta}$-rich core–shell nanoparticles on 3D ordered macroporous $Ce_{1-x}Zr_xO_2$ for soot oxidation: Nanostructure-dependent catalytic activity. *Nanoscale* **2017**, *9*, 4558–4571. [CrossRef] [PubMed]
17. Li, Y.; Du, Y.; Wei, Y.; Zhao, Z.; Jin, B.; Zhang, X.; Liu, J. Catalysts of 3D ordered macroporous ZrO_2-supported core–shell Pt@CeO_{2-x} nanoparticles: Effect of the optimized Pt–CeO_2 interface on improving the catalytic activity and stability of soot oxidation. *Catal. Sci. Technol.* **2017**, *7*, 968–981. [CrossRef]
18. Oh, S.H.; Hoflund, G.B. Chemical state study of palladium powder and ceriasupported Palladium during low-temperature CO oxidation. *J. Phys. Chem. A* **2006**, *110*, 7609–7613. [CrossRef]
19. Wang, L.; Deo, S.; Mukhopadhyay, A.; Pantelis, N.A.; Janik, M.J.; Rioux, R.M. Emergent behavior in oxidation catalysis over single-atom Pd on a reducible CeO_2 support via mixed redox cycles. *ACS Catal.* **2022**, *12*, 12927–12941. [CrossRef]
20. Yoo, S.; Lee, E.; Jang, G.H.; Kim, D.H. Effect of Pd precursors on the catalytic properties of Pd/CeO_2 catalysts for CH_4 and CO oxidation. *Mol. Catal.* **2022**, *533*, 112791. [CrossRef]
21. Song, W.; Hensen, E.J.M. Mechanistic aspects of the water-gas shift reaction on isolated and clustered Au atoms on CeO_2(110): A density functional theory study. *ACS Catal.* **2014**, *4*, 1885–1892. [CrossRef]

22. Song, W.; Hensen, E.J.M. A computational DFT study of CO oxidation on a Au nanorod supported on CeO_2(110): On the role of the support termination. *Catal. Sci. Technol.* **2013**, *3*, 3020–3029. [CrossRef]
23. Xing, M.; Guo, L.; Hao, Z. Theoretical study of the single noble metal stabilized on metal oxide clusters catalyze the water-gas shift reaction. *Int. J. Quantum Chem.* **2018**, *118*, e25767. [CrossRef]
24. Zhang, W.; Pu, M.; Lei, M. Theoretical studies on the stability and reactivity of the metal-doped CeO_2(100) surface: Toward H_2 dissociation and oxygen vacancy formation. *Langmuir* **2020**, *36*, 5891–5901. [CrossRef] [PubMed]
25. Lee, M.W.; Lee, E.J.; Lee, K.Y. Comparative analysis of NO_x reduction on Pt, Pd, and Rh catalysts by DFT calculation and microkinetic modeling. *Appl. Surf. Sci.* **2023**, *611*, 155572. [CrossRef]
26. Thang, H.V.; Pham, T.L.M. DFT insights into the electronic structure of Rh single-atom catalysts stabilized on the CeO_2(1 1 1) surface. *Chem. Phys. Lett.* **2022**, *803*, 139810. [CrossRef]
27. Cao, X.S.; Zhang, C.X.; Wang, Z.; Liu, W.; Sun, X.M. Surface reduction properties of ceria-zirconia solid solutions: A first-principles study. *RSC Adv.* **2020**, *10*, 4664–4671. [CrossRef]
28. Tian, D.; Li, K.; Wei, Y.; Zhu, X.; Zeng, C.; Cheng, X.; Zheng, Y.; Wang, H. DFT insights into oxygen vacancy formation and CH_4 activation over CeO_2 surfaces modified by transition metals (Fe, Co and Ni). *Phys. Chem. Chem. Phys.* **2018**, *20*, 11912–11929. [CrossRef]
29. Tian, D.; Zeng, C.; Wang, H.; Cheng, X.; Zheng, Y.; Xiang, C.; Wei, Y.; Li, K.; Zhu, X. Effect of transition metal Fe adsorption on CeO_2(110) surface in the methane activation and oxygen vacancy formation: A density functional theory study. *Appl. Surf. Sci.* **2017**, *416*, 547–564. [CrossRef]
30. Cao, X.S.; Zhang, C.X.; Dong, F.S.; Sun, X.M. Mechanistic insight into the selective catalytic reduction of NO_x with propene on the $Ce_{0.875}Zr_{0.125}O_2$ (110) surface. *Catal. Sci. Technol.* **2022**, *12*, 3685–3694. [CrossRef]
31. Yang, M.L.; Zhu, Y.A.; Fan, C.; Sui, Z.J.; Chen, D.; Zhou, X.G. Density functional study of the chemisorption of C1, C2 and C3 intermediates in propane dissociation on Pt(1 1 1). *J. Mol. Catal. A Chem.* **2010**, *321*, 42–49. [CrossRef]
32. Valcárcel, A.; Ricart, J.M.; Clotet, A.; Markovits, A.; Minot, C.; Illas, F. Theoretical study of the structure of propene adsorbed on Pt(111). *Surf. Sci.* **2002**, *519*, 250–258. [CrossRef]
33. Wu, T.; Guo, R.T.; Li, C.F.; Pan, W.G. Recent progress of CeO_2-based catalysts with special morphologies applied in air pollutants abatement: A review. *J. Environ. Chem. Eng.* **2023**, *11*, 109136. [CrossRef]
34. Aneggi, E.; Llorca, J.; Boaro, M.; Trovarelli, A. Surface-structure sensitivity of CO oxidation over polycrystalline ceria powders. *J. Catal.* **2005**, *234*, 88–95. [CrossRef]
35. Huang, M.; Fabris, S. CO adsorption and oxidation on ceria surfaces from DFT+U calculations. *J. Phys. Chem. C* **2008**, *112*, 8643–8648. [CrossRef]
36. Song, W.; Su, Y.; Hensen, E.J.M. A DFT study of CO oxidation at the Pd–CeO_2(110) interface. *J. Phys. Chem. C* **2015**, *119*, 27505–27511. [CrossRef]
37. Delley, B. An all-electron numerical method for solving the local density functional for polyatomic molecules. *J. Chem. Phys.* **1990**, *92*, 508–517. [CrossRef]
38. Delley, B. From molecules to solids with the $DMol^3$ approach. *J. Chem. Phys.* **2000**, *113*, 7756–7764. [CrossRef]
39. Perdew, J.P.; Burke, K.; Ernzerhof, M. Generalized gradient approximation made simple. *Phys. Rev. Lett.* **1996**, *77*, 3865–3868. [CrossRef]
40. Bergner, A.; Dolg, M.; Küchle, W.; Stoll, H.; Preuß, H. Ab initio energy-adjusted pseudopotentials for elements of groups 13–17. *Mol. Phys.* **1993**, *80*, 1431–1441. [CrossRef]
41. Nolan, M.; Grigoleit, S.; Sayle, D.; Parker, S.; Watson, G. Density functional theory studies of the structure and electronic structure of pure and defective low index surfaces of ceria. *Surf. Sci.* **2005**, *576*, 217–229. [CrossRef]
42. Da Silva, J.L.; Ganduglia-Pirovano, M.V.; Sauer, J.; Bayer, V.; Kresse, G. Hybrid functionals applied to rare-earth oxides: The example of ceria. *Phys. Rev. B* **2007**, *75*, 045121. [CrossRef]
43. Zhao, L.; Wu, Y.W.; Han, J.; Lu, Q.; Yang, Y.P.; Zhang, L.B. Mechanism of mercury adsorption and oxidation by oxygen over the CeO_2 (111) Surface: A DFT Study. *Materials* **2018**, *11*, 485. [CrossRef] [PubMed]
44. Halgren, T.A.; Lipscomb, W.N. The synchronous-transit method for determining reaction pathways and locating molecular transition states. *Chem. Phys. Lett.* **1977**, *49*, 225–232. [CrossRef]